

Fault Recovery and Transient Stability of Grid-Forming Converters Equipped with Current Saturation

Ali Arjomandi-Nezhad, *Student Member, IEEE*, Yifei Guo, *Member, IEEE*, Bikash C. Pal, *Fellow, IEEE*, Guangya Yang, *Senior Member, IEEE*,

Abstract—When grid-forming (GFM) inverter-based resources (IBRs) experience large grid disturbances (e.g., short-circuit faults), the current limiter may be triggered and GFM IBRs enter the current saturation mode, inducing nonlinear dynamical behaviors and imposing great challenges to the post-disturbance transient angle stability. This paper presents a systematic study to reveal the fault recovery behaviors of a GFM IBR and identify the risk of instability. The impact of the angle of the magnitude-saturated current on the post-fault recovery and transient stability is also investigated. The selection of the angle of magnitude-saturated current significantly influences the post-fault behaviors while a few additional dynamical conditions that have a substantial impact are also identified. It is found that the system may follow multiple post-fault recovery trajectories depending on those conditions: 1) Convergence to the normal stable equilibrium point (SEP), 2) convergence to the saturated stable equilibrium point (SSEP), and 3) divergence (instability). To examine the models' accuracy, several cases are simulated.

Index Terms—current limiter, current saturation, grid-forming (GFM) converters, post-fault recovery, transient stability, virtual synchronous generator (VSG).

I. INTRODUCTION

RETIREMENT of conventional synchronous generator-based power plants in favor of inverter-based resources (IBRs) made it necessary to implement grid-forming (GFM) control to provide various services, e.g. frequency and voltage support [1]–[4]. Nevertheless, GFM IBRs equipped with the current limitation/saturation exhibit complicated nonlinear dynamics during and after large disturbances [5], affecting the system stability. Therefore, it is vital to study and model their responses to large disturbances.

The ability of GFM IBRs to retain synchronism with the grid after being subjected to a large disturbance is defined as their transient stability [6]. Since a GFM IBR usually synchronizes itself to the grid through the active power controller (APC), its transient stability can be redefined as the stability of the APC around the stable equilibrium point (SEP) [4]. Several papers studied the transient stability of GFM IBRs around the SEP by adopting Lyapunov-based methods

[7], [8], Krylov–Bogoliubov–Mitropolsky (KBM) asymptotic method [9], quantitative parameters constraining [10], [11], and damping energy visualization and geometry approximation [12]. However, these papers neglected the impact of current saturation on the dynamics of GFM IBRs. Unlike SGs, IBRs usually have rather limited overcurrent capability. For example, this limitation for Type IV Wind Turbine Generators is 110 % to 120 % nominal [13], which is very easy to hit during disturbances. It has been demonstrated in the literature that the current saturation adversely affects the transient stability [4], [5].

A few papers considered the current limiter in transient stability analysis. Generally, there are two categories of current limitation methods [14]: virtual impedance (VI) and current reference saturation (CRS). The former reduces the GFM voltage reference, whereas the latter directly limits the current reference generated by the voltage controller. References [15]–[17] studied transient stability of the VI-based current-saturated GFM IBRs. Although the VI-based methods preserve the voltage source behavior, they may fail to limit the current within the first few milliseconds [14], [18]. In contrast, CRS-based methods limit the current promptly. Activation of CRS causes GFM IBRs to act as a current source while still being synchronized to the grid through the active power controller.

The authors of [19] calculated the post-fault domain of attraction (DOA) for transient stability of GFM IBRs considering d-priority CRS. Reference [20] analyzed the transient stability of a GFM IBR equipped with q-priority CRS. Authors of [21] pointed out the existence of a saturated stable equilibrium point (SSEP). According to [21], if the angle of SSEP is more than the saturation angle threshold, the GFM IBR might be locked into the current-saturation mode after a fault. Nevertheless, as will be shown later in this paper, there exists another circumstance for converging to the SSEP. To explore circumstances in which a GFM IBR is locked into SSEP, the conditions to enter and return from the current-saturation mode should be identified. Reference [22] discussed that these two conditions are functions of the angle of the converter's reference dq-frame from the grid's Thevenin voltage angle. It introduced (a) the set of returning angles as the set of angles in which the voltage controller generates a current reference less than the allowable amount if it is in the current-saturated operation mode and (b) the set of entering angles as the set of angles in which the GFM IBR transits from normal operation mode to the current-saturation mode. Formulations for the

This work was supported in part by the European Union's Horizon 2020 Research and Innovation Programme under the Marie Skłodowska-Curie Grant 956433 (InnoCyPES Project), in part by the Resilient Operation of Sustainable Energy Systems (ROSES) U.K.-China (EPSRC-NSFC) Programme on Sustainable Energy Supply under Grants EP/T021713/1 and NSFC-52061635102, and in part by the Royal Society under Grant RG\R2\232398. For the purpose of open access, the authors have applied a Creative Commons Attribution (CC BY) license to any Accepted Manuscript version arising.

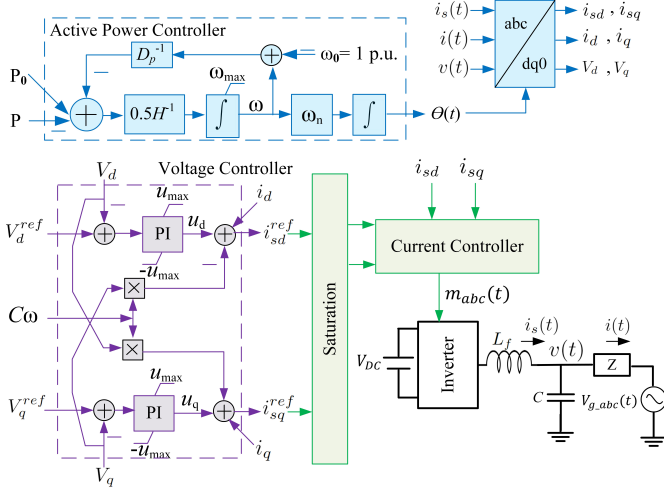


Fig. 1. The structure of a three-layer VSG GFM IBR [4], [23].

set of entering angles have been extensively presented in the literature, e.g. [4]. However, an analytical approach for the set of returning angles has not been attempted.

To the best of our knowledge, a closed-form expression for the set of returning angles and a comprehensive analysis of the situations in which a GFM IBR is locked into the current-saturation mode after disturbances are missing in the literature. To bridge this gap, this paper first identifies conditions under which a GFM IBR returns from the current-saturation mode. All the circumstances under which a GFM IBR converges to the SSEP are also explored in this paper. All formulations and analyses provided in this paper are valid for different X/R ratios. The main contributions of this paper are:

- A formulation for the set of returning angles is derived. It is proven that this set is a function of the angle of the magnitude-saturated current (mentioned as saturated current in the rest of the paper).
- The circumstances in which a GFM IBR is locked into the SSEP are investigated.
- The influence of various parameters, such as the saturated current angle and the X/R ratio of grid impedance on post-fault recovery and transient stability, is analyzed.

The rest of the paper is organized as follows. Section II presents a general overview of multi-loop virtual synchronous generator (VSG) GFM IBRs. Section II investigates situations in which a GFM IBR enters into or returns from the current-saturation mode. The model of a GFM IBR in the current-saturation mode is also reviewed in Section II. The model of transient stability of a VSG considering CRS is provided in Section IV. Circumstances that a GFM IBR is locked into the current-saturation mode are also explored in Section IV. A sensitivity analysis on the effect of the grid's conditions and controller's parameters on transient stability is provided in Section V. The case studies are presented in Section VI followed by conclusions.

II. SYSTEM STRUCTURE

There are several control structures for GFM IBRs in the literature. This paper considers a typical three-level VSG as

shown in Fig. 1 [4]. The inverter is connected to the grid, which is modeled as a Thevenin equivalent of voltage \vec{V}_g and impedance of $R_g + jX_g$, through a transformer with the impedance $R_{tr} + jX_{tr}$ and an LC filter with inductance of L_f and capacitance of C . The total equivalent impedance from IBR terminal is $(R_g + jX_g) + (R_{tr} + jX_{tr}) = R + jX = Ze^{j\phi}$. Since the filter capacitance is small, its effect is neglected in the rest of the paper.

The inverter is controlled through a three-level hierarchical control containing the outer layer, the inner layer, and the innermost layer shown with colors blue, purple, and green in Fig. 1, respectively. The outer layer consists of APC, which emulates the second order swing equation [24], and reactive power controller (RPC), which controls the reactive power by setting a reference magnitude for the voltage [2]. Since RPC is not the focus of this paper, it is not shown in Fig. 1, and we assume that it always generates the nominal voltage reference. APC generates the frequency and angle for the converter's reference dq-frame. The difference between the angle of dq-frame and the angle of \vec{V}_g is called APC angle [$\delta = \theta(t) - \theta_g(t)$] and plays a critical role in keeping the GFM IBR synchronous with the grid. The inner controller includes the voltage controller which controls the terminal voltage \vec{V} to be aligned with the d-axis with the magnitude of V_d^{ref} . This controller generates the current reference for the current controller, which is the innermost control layer. The GFM IBR acts as a voltage source unless the magnitude of the current reference exceeds I_s^{max} . In this situation, the saturation block gives the saturated current reference to the current controller, and the GFM IBR behaves as a current source.

III. CURRENT-SATURATION OPERATION MODE

When the GFM IBR operates in the normal operation mode, its terminal voltage aligns with the d-axis and has the magnitude of V_d^{ref} as shown in Fig. 2(a). In this situation, the active power output is expressed as

$$P_{\text{unsat}} = \frac{(V_d^{\text{ref}})^2}{Z} \sin \alpha + \frac{V_g V_d^{\text{ref}}}{Z} \sin(\delta - \alpha) \quad (1)$$

where $\delta = \theta(t) - \theta_g(t)$ is the APC angle, which is the angle between the converter's dq-frame and grid's Thevenin voltage, and $\alpha = \arctan(R/X)$. If there is a deep voltage sag Fig. 2(b) or excessive APC angle Fig. 2(c), the GFM IBR is no longer able to regulate the terminal voltage to \vec{V}_{ref} subject to the current limit [4]. Consequently, the saturation block gives the saturated current reference $(I_s^{\text{max}} \cos(\beta), I_s^{\text{max}} \sin(\beta))$ to the current controller, where β is the saturated current angle with respect to the converter's reference d-axis. In this situation, $(V_d, V_q) \neq (V_d^{\text{ref}}, 0)$ as depicted in Fig. 2 (d). Neglecting the impact of the filter capacitor, the terminal voltage of the IBR under the converter's reference dq-frame is given by [4]

$$V_d^{\text{sat}} = V_g \cos \delta + Z I_s^{\text{max}} \sin(\alpha - \beta) \quad (2)$$

$$V_q^{\text{sat}} = -V_g \sin \delta + Z I_s^{\text{max}} \cos(\alpha - \beta). \quad (3)$$

Since terminal voltage is not aligned with the d-axis, saturated current angle β should not be confused with the power factor

angle. The power factor angle, which is the angle between voltage and current phasors, is $\arctan(V_q^{\text{sat}}/V_d^{\text{sat}}) - \beta$.

The active power output during the current-saturation operation mode follows

$$P_{\text{sat}} = R(I_s^{\text{max}})^2 + V_g I_s^{\text{max}} \cos(\delta + \beta). \quad (4)$$

Accordingly, the power depends on both δ and β . Hence, the influence of β on transient stability is evident based on the strong coupling between transient stability and active power. This influence will be detailed later in Sections IV and V.

A. Sets of Entering and Returning Angles

The GFM IBR enters the current-saturation mode [4] if

$$\cos(\delta) \leq \frac{1}{2} \left(\frac{V_d^{\text{ref}}}{V_g} + \frac{V_g}{V_d^{\text{ref}}} - \frac{(ZI_s^{\text{max}})^2}{V_g V_d^{\text{ref}}} \right). \quad (5)$$

Defining the saturation threshold angle as δ_{sat} as

$$\delta_{\text{sat}} = \arccos \left(\frac{1}{2} \left(\frac{V_d^{\text{ref}}}{V_g} + \frac{V_g}{V_d^{\text{ref}}} - \frac{(ZI_s^{\text{max}})^2}{V_g V_d^{\text{ref}}} \right) \right), \quad (6)$$

the set of entering angles (denoted \mathcal{S}), where all APC angles satisfying the condition (5), is given by

$$\mathcal{S} = [-180^\circ, -\delta_{\text{sat}}] \cup [\delta_{\text{sat}}, 180^\circ]. \quad (7)$$

Equation (7) confirms the discussion earlier in this section that a GFM IBR goes to the current-saturation mode if the absolute value of the APC angle δ exceeds a threshold. This threshold depends on the grid voltage as analyzed in [4] in detail.

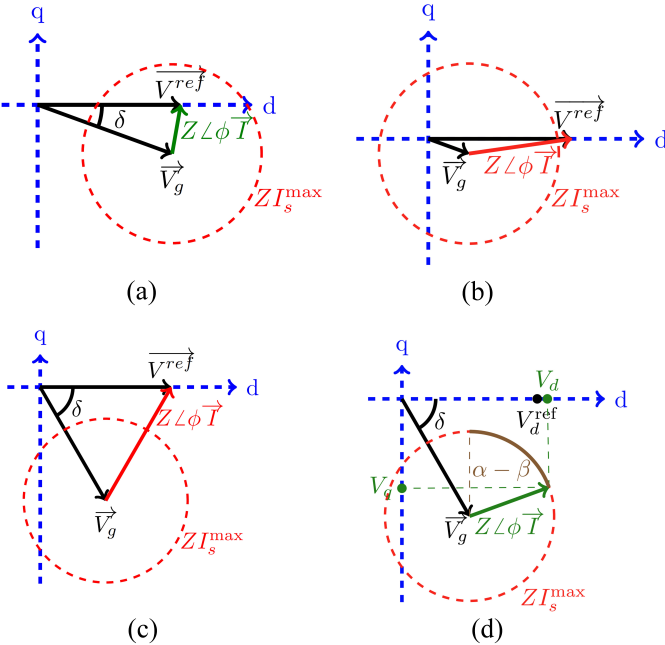


Fig. 2. Phasor-Diagram of the voltages in (a) steady-state normal operation mode, (b) voltage sag, (c) extra APC angle, and (d) extra APC angle with CRS.

As soon as the APC angle exits \mathcal{S} , the voltage controller of GFM IBR should generate a current reference less than the maximum allowable value, and the GFM IBR should come back to the normal operation mode. However, this may not be true under certain circumstances. The set of APC angles at which the GFM IBR can return to the normal operation mode spontaneously is expressed as

$$\mathcal{R} = \left\{ -180^\circ \leq \delta \leq 180^\circ \mid (i_{sd}^{\text{ref}})^2 + (i_{sq}^{\text{ref}})^2 \leq (I_s^{\text{max}})^2 \right\} \quad (8)$$

where i_{sd}^{ref} and i_{sq}^{ref} are functions of the terminal voltage, which is, in turn, a function of δ . These two references are unsaturated immediate outputs of the voltage controller.

One of the main goals of this work is to delve into $\mathcal{R}(\beta)$ by solving (8). The current reference is given by [23]:

$$i_{sd}^{\text{ref}} = u_d - yV_q + i_d \approx u_d + I_s^{\text{max}} \cos \beta \quad (9)$$

$$i_{sq}^{\text{ref}} = u_q + yV_d + i_q \approx u_q + I_s^{\text{max}} \sin \beta \quad (10)$$

where $y = C\omega$ is the filter shunt admittance, and u_d and u_q are the outputs of the PI voltage controller depicted in Fig. 1. By substituting (9) and (10) into (8), it can be rewritten as

$$(u_d + I_s^{\text{max}} \cos \beta)^2 + (u_q + I_s^{\text{max}} \sin \beta)^2 \leq (I_s^{\text{max}})^2. \quad (11)$$

In the current-saturation mode, u_d and u_q are either u_{max} or $-u_{\text{max}}$ depending on the sign of the error signals $V_d^{\text{ref}} - V_d$ and $V_q^{\text{ref}} - V_q$ where $V_q^{\text{ref}} = 0$. Therefore, equation (11), which is the condition for returning to the normal operation mode, can be rewritten as

$$\text{sign}(u_d) \cos \beta + \text{sign}(u_q) \sin \beta \leq -\frac{u_{\text{max}}}{I_s^{\text{max}}}. \quad (12)$$

u_d and u_q are zero in steady-state. Therefore, u_{max} is set to a small value alongside the clamping anti-windup method to prevent voltage controller windup when it faces large disturbances. If $u_{\text{max}} \ll I_s^{\text{max}}$, the right-hand side of (12) is close to zero. The set of the saturated current angle β , which satisfies (12), is presented in Table I.

According to Table I, for $-45^\circ \leq \beta \leq 0^\circ$, (12) is satisfied if u_d is negative. Signals u_d and u_q have the same sign with the voltage controller's error signals, i.e. $V_d^{\text{ref}} - V_d$ and $-V_q$, respectively. According to (2), this is equivalent to $-\delta_d^p(\beta) \leq \delta \leq \delta_d^p(\beta)$, where $\delta_d^p(\beta)$ is defined as

$$\delta_d^p(\beta) = \arccos \left(\frac{V_d^{\text{ref}} - ZI_s^{\text{max}} \sin(\alpha - \beta)}{V_g} \right). \quad (13)$$

On the other hand, for $-90^\circ \leq \beta \leq -45^\circ$, (12) is satisfied if u_q is positive, which means $-V_q > 0$. According to (3),

TABLE I
THE SETS OF β SATISFYING (12)

	$\text{sign}(u_d) > 0$	$\text{sign}(u_d) < 0$
$\text{sign}(u_q) > 0$	$-90^\circ \leq \beta \leq -45^\circ$	$-90^\circ \leq \beta \leq 0^\circ$
$\text{sign}(u_q) < 0$	\emptyset	$-45^\circ \leq \beta \leq 0^\circ$

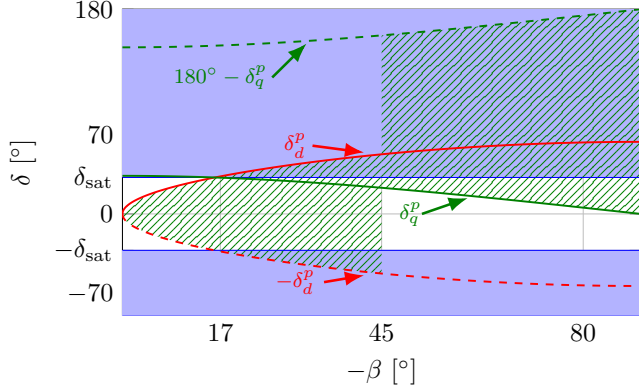


Fig. 3. Graphical representation of entering and returning sets with solid and hashed fill areas, respectively if $\alpha = 0$ and $Z = 0.46$ p.u.

this is equivalent to $\delta_q^p(\beta) \leq \delta \leq 180^\circ - \delta_q^p(\beta)$, where $\delta_q^p(\beta)$ is defined as

$$\delta_q^p(\beta) = \arcsin\left(\frac{ZI_s^{\max} \cos(\alpha - \beta)}{V_g}\right). \quad (14)$$

Therefore, the set $\mathcal{R}(\beta)$ depends on β , that is,

$$\mathcal{R}(\beta) = \begin{cases} [-\delta_d^p(\beta), \delta_d^p(\beta)], & \beta \in [-45^\circ, 0^\circ] \\ [\delta_q^p(\beta), 180^\circ - \delta_q^p(\beta)], & \beta \in [-90^\circ, -45^\circ]. \end{cases} \quad (15)$$

When $\beta \in [-45^\circ, 0^\circ]$, the dominant component of the current reference is i_{sd}^{ref} , which is positive. If $u_d < 0$, the magnitude of the current reference becomes smaller than the maximum value according to (9) and (11). When $\beta \in [-90^\circ, -45^\circ]$, i_{sq}^{ref} , which is negative, is the dominant component of the current reference. If $u_q > 0$, the magnitude of the current reference becomes smaller than the maximum value according to (10) and (11).

When $\delta \in \mathcal{S}$, the current needed for adjusting the voltage to the voltage reference $\vec{V}_{\text{ref}} = (V_d^{\text{ref}}, 0)$ is more than the limit, and current saturation happens since the voltage controller generates a reference more than the allowed value. During the current-saturation operation mode, if $\delta \in \mathcal{R}$, the magnitude of the current reference generated by the voltage controller decreases below the threshold. Consequently, the GFM IBR switches to the normal operation mode. Hence, depending on the APC angle, the GFM IBR might exhibit different post-fault behaviors:

- $\delta \in \mathcal{S} - \mathcal{R}(\beta)$: The GFM IBR operates in the current-saturation mode [22]. It is shown with the solid filled area in Fig. 3.
- $\delta \in \mathcal{R}(\beta) - \mathcal{S}$: The GFM IBR operates in the normal operation mode [22]. The hashed area in Fig. 3 represents this subset.
- $\delta \in \mathcal{R}(\beta) \cap \mathcal{S}$: The GFM IBR oscillates between normal operation and current-saturation modes [22]. This subset is shown as the intersection of the solid filled area and hashed area in Fig. 3. These oscillations can be reduced using the forced saturation introduced in [4].

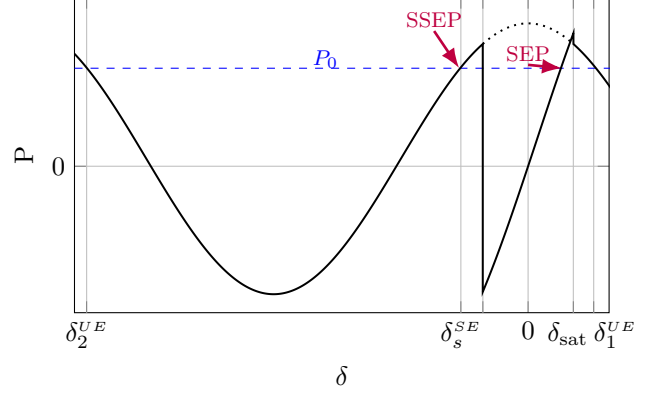


Fig. 4. Power-Angle curve for a GFM IBR equipped with the CRS.

- $\delta \notin \mathcal{R}(\beta) \cup \mathcal{S}$: The GFM IBR retains its mode. The white area in Fig. 3 represents this situation. If the GFM IBR was already in the current-saturation mode, it remains in the current-saturation mode even though the post-disturbance APC angle $\delta_{af} \notin \mathcal{S}$.

IV. TRANSIENT STABILITY OF GFM IBRS

The GFM IBR synchronizes itself to the grid through APC, which follows the second-order swing equation [24] if it is designed as a VSG:

$$P_0 - P = 2H \frac{d\omega}{dt} + \frac{1}{D_p} (\omega - \omega_0) \quad (16)$$

$$\frac{d\delta}{dt} = \omega_n (\omega - \omega_0) \quad (17)$$

where H , D_p , P_0 , ω_0 , and ω_n are virtual inertia, active droop coefficient, active power reference, set-point frequency, and the nominal frequency, respectively. These equations outline the strong tie between the trajectory of the APC and the active power, which follows (1) and (4) for the normal and the current-saturation operation modes, respectively. The intersections of the power-angle curve and the power reference, shown in Fig. 4, form equilibrium points which are:

- SEP: This is the normal stable equilibrium point to which convergence is desired. Deduced from (1), it is calculated as

$$\delta^{SE} = \alpha + \arcsin\left(\frac{Z}{V_g V_d^{\text{ref}}}\left(P_0 - \frac{(V_d^{\text{ref}})^2}{Z} \sin(\alpha)\right)\right). \quad (18)$$

- Unstable Equilibrium 1 ($\delta_1^{UE}(\beta)$): If the APC angle reaches this value while $\omega > \omega_0$, the GFM IBR loses its synchronism with the grid. Based on (4), it is calculated as

$$\delta_1^{UE}(\beta) = -\beta + \arccos\left(\frac{P_0 - R(I_s^{\max})^2}{V_g I_s^{\max}}\right). \quad (19)$$

It shows that decreasing β increases the $\delta_1^{UE}(\beta)$ which helps transient stability by pushing away the unstable equilibrium point.

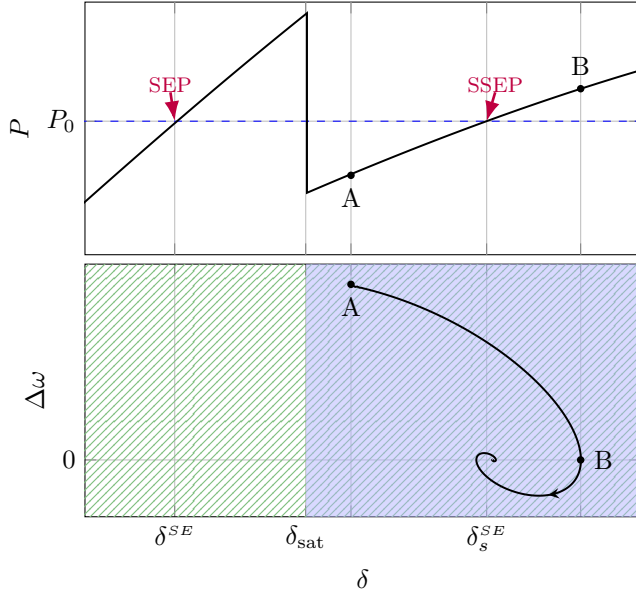


Fig. 5. Post-fault trajectory and active power for the case where C_1 holds.

- Unstable Equilibrium 2 ($\delta_2^{UE}(\beta)$): The GFM IBR loses its synchronism if the APC angle reaches this value while $\omega < \omega_0$. According to (4), this angle is calculated as

$$\delta_2^{UE}(\beta) = \delta_1^{UE}(\beta) - 360^\circ. \quad (20)$$

- SSEP ($\delta_s^{SE}(\beta)$): It is the stable intersection between the power reference and power output in the current-saturation mode. Deduced from (4), it is calculated as

$$\delta_s^{SE}(\beta) = -\beta - \arccos\left(\frac{P_0 - R(I_s^{\max})^2}{V_g I_s^{\max}}\right). \quad (21)$$

It has been discussed in [21] that if $\delta_{\text{sat}} \leq \delta_s^{SE}(\beta)$, the SSEP has a DOA that causes locking in the saturation mode. It will be discussed in the following subsection that there is another condition for locking into the saturation mode.

A. Converging to the Saturated Stable Equilibrium Point

A GFM IBR is locked into the current-saturation mode if it converges to the SSEP before it returns to the normal operation mode. It has been shown in [21] that if $\delta_s^{SE}(\beta) \in \mathcal{S}$ and the post-fault APC angle $\delta_{af} \in \mathcal{S}$, the post-fault trajectory might converge to the SSEP. This condition, which is denoted as C_1 here, is not the only circumstance for converging into SSEP. Since the set of returning angles $\mathcal{R}(\beta)$ is not exactly the complement of the set of entering angles \mathcal{S} , there are cases that even though $\delta_s^{SE}(\beta) \notin \mathcal{S}$, the GFM IBR is locked into the current-saturation mode. It happens if the initial post-fault APC angle δ is out of the set of returning angles, and does not enter this set while passing its trajectory to the SSEP which is out of the set of returning angles in addition to being excluded from \mathcal{S} . It is denoted as C_2 here as the combination of the following conditions: (a) $\delta_s^{SE}(\beta) \notin \mathcal{R}(\beta) \cup \mathcal{S}$, (b) the post-fault trajectory toward $\delta_s^{SE}(\beta)$ does not enter the set of

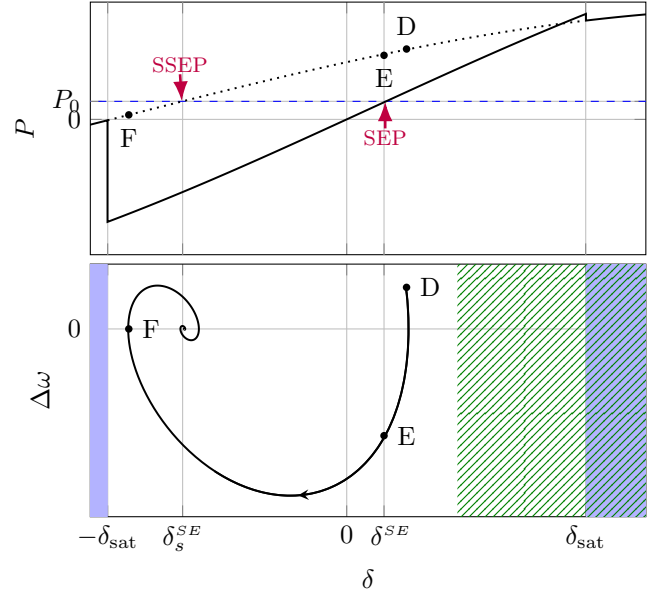


Fig. 6. Post-fault trajectory and active power output for a scenario that condition C_2 meets. The dotted curve is the power output in the current-saturation mode while $\delta \notin \mathcal{S}$.

returning angles $\mathcal{R}(\beta)$, and (c) the GFM IBR does not lose synchronism with the grid. This set of conditions is expressed as

$$C_2 : \begin{cases} \delta_s^{SE}(\beta) \notin \mathcal{R}(\beta) \cup \mathcal{S} & (C_{21}) \\ \delta(t) \notin \mathcal{R}(\beta), \forall t & (C_{22}) \\ \delta_2^{UE}(\beta) < \delta(t) < \delta_1^{UE}(\beta), \forall t & (C_{23}) \end{cases} \quad (22)$$

where C_{21} is an static condition, C_{22} and C_{23} are dynamic conditions.

Fig. 5 and 6 depict two cases of converging into the SSEP for a GFM IBR with $D_p = 0.03$ p.u. connected to a Grid with the equivalent impedance of $Z = 0.46$ p.u. and $X/R = 20$. In these figures, the solid filled area represents the \mathcal{S} and the hashed area represents $\mathcal{R}(\beta)$. The GFM IBR is forced to be in the current-saturation mode if $\delta \in \mathcal{S} \cap \mathcal{R}(\beta)$ as it was proposed in [4]. The convergence to SSEP in Fig. 5 is due to C_1 . In this case, SSEP belongs to the set of entering to saturation angles and contains point A in its DOA. On the other hand, C_2 causes locking into the saturation mode in Fig. 6. SSEP is out of \mathcal{S} . However, since the post-fault angle (δ_D) is out of $\mathcal{R}(\beta)$, the GFM IBR does not come back to the normal operation mode. The post-fault trajectory of the GFM IBR until the convergence to SSEP does not pass a point in $\mathcal{R}(\beta)$. According to Fig. 6, the GFM IBR does not converge to the SEP even though the post-fault state D is close to SEP. The fulfillment of condition C_2 imposes a significant challenge as even relatively small disturbances might also lead to undesired consequences.

Since both $\delta_s^{SE}(\beta)$ and $\mathcal{R}(\beta)$ are functions of the saturated current angle β , the proper selection of β can eliminate the risk of locking into the current-saturation mode through C_1 or C_2 . If $\delta_s^{SE}(\beta) \in \mathcal{R}(\beta) - \mathcal{S}$, the GFM IBR is not locked into the current-saturation mode. This is because of the fact that

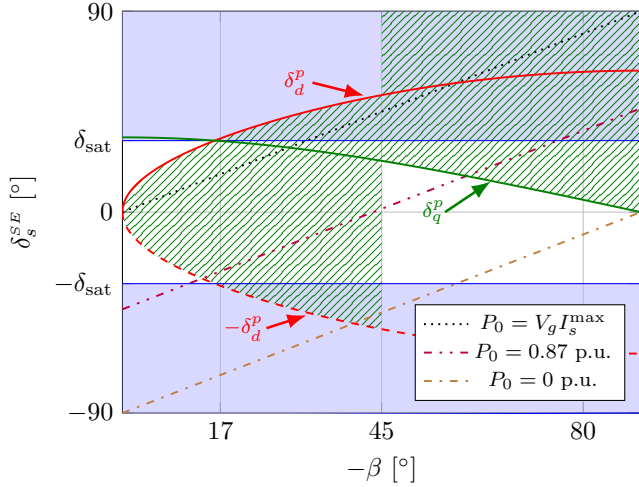


Fig. 7. Relation between the SSEP angle and β . Solid filled area represents S and hashed area shows $\mathcal{R}(\beta)$.

the GFM IBR comes back to the normal operation mode at the angle of SSEP. $\delta_s^{SE}(\beta)$ depends on the power reference in addition to β as demonstrated in Fig. 7. Therefore, β satisfying the mentioned condition differs for different power references. Hence, an adaptive β selection is needed to mitigate or decrease the risk of converging into the SSEP.

To avoid the complexity in Section V, it is assumed that $\mathcal{R}(\beta)$ and \mathcal{S} are complements. Therefore, condition \mathcal{C}_2 is not analyzed in Section V. This assumption is made only in that section. Later, cases that these two sets are not complements are analyzed in the Case Study section.

V. EFFECT OF PARAMETERS ON TRANSIENT STABILITY

It has been discussed in [4] that the current saturation deteriorates the post-fault by decreasing the acceleration area and the angle of the positive equilibrium point. This decrement depends on β in addition to APC control parameters and grid parameters because β affects the active power as demonstrated in Fig. 8. This figure depicts that a smaller β leads to a shift in

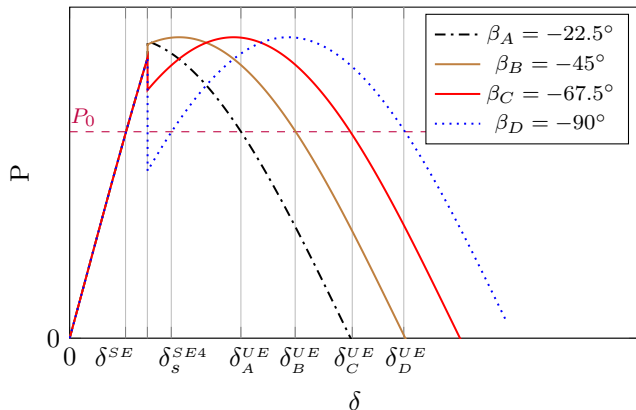


Fig. 8. Power-Angle curves for different saturated current angles β .

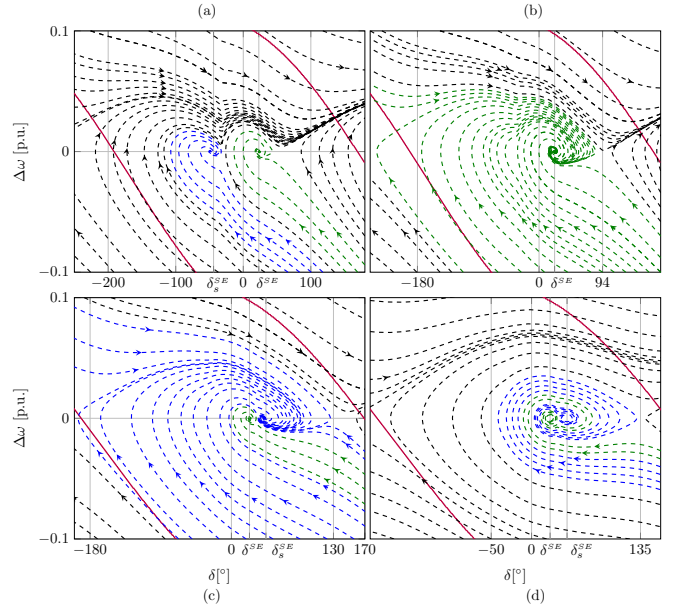


Fig. 9. Phase portraits for a GFM IBR connected to an equivalent impedance of $Z = 0.46$ p.u., and $\alpha = 5.71^\circ$, and β equals to (a) 0° , (b) -45° , (c) -90° , and (d) -90° . D_p is equal to 0.03 p.u. for (a)-(c) and 0.09 p.u. for (d). Purple lines are borders of DOA for unsaturated GFM IBRs.

unstable equilibrium point and an increase in deceleration area compared to a bigger β . However, if β exceeds a limitation, there exists an SSEP in \mathcal{S} , which might cause locking in the current-saturation mode through the condition \mathcal{C}_1 .

Fig. 9 shows post-disturbance transient phase portraits for different saturated current angles. β is zero in Fig. 9(a). The SSEP attracts a subset of the state-space under the condition \mathcal{C}_1 . In Fig. 9(b), β is -45° . Thus, SSEP is out of \mathcal{S} , and \mathcal{C}_1 cannot hold. The DOA of SEP is considerably bigger than that of Fig. 9(a). The saturated current angle is -90° in Fig. 9(c). As depicted in this phase portrait, DOA of the SSEP is considerably bigger than DOA of the SEP. If the droop coefficient increases from 0.03 p.u. to 0.09 p.u., the DOAs of these two equilibrium points become hardly separable as shown in Fig. 9(d). Therefore, it is crucial to set β in a way to exclude the SSEP from \mathcal{S} . So that the condition \mathcal{C}_1 is not met.

Other main effecting parameters are the droop coefficient, X/R ratio, and the total impedance Z , which are analyzed in detail in the rest of this section. All DOAs are assessed through the numerical calculation of trajectories based on the swing equation and saturated and unsaturated active powers. β in these cases is -45° so that condition \mathcal{C}_1 does not hold.

Decreasing the droop coefficient provides more damping to the swing equation (16). Therefore, an expanded DOA is expected, which is verified in Fig. 10.

The total impedance Z and X/R ratio shape the relation between the power and angle. Therefore, they influence the dynamics of APC. Fig. 11 depicts that the power output in the current-saturation mode is more for resistive grid impedance compared to inductive grids. Furthermore, the positive unstable equilibrium point is shifted away. Therefore, DOA of SEP

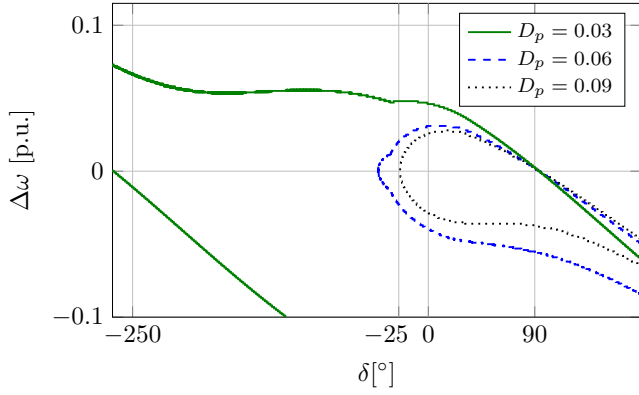


Fig. 10. Borders of DOAs for different droop coefficients where the equivalent impedance is 0.46 p.u. and $\alpha = 5.71^\circ$.

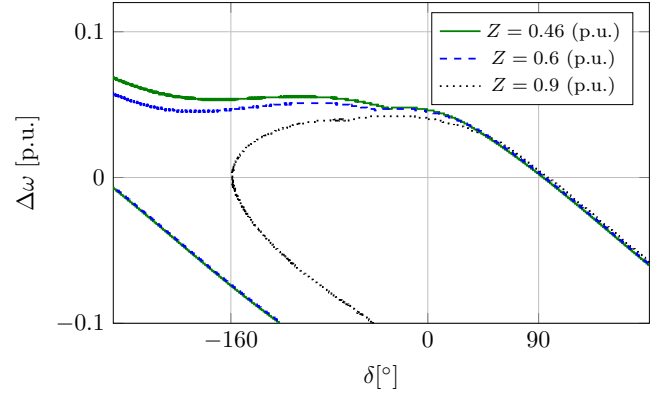


Fig. 13. Borders of DOAs for different total impedances. $\alpha = 5.71^\circ$, and $D_p = 0.03$ p.u.

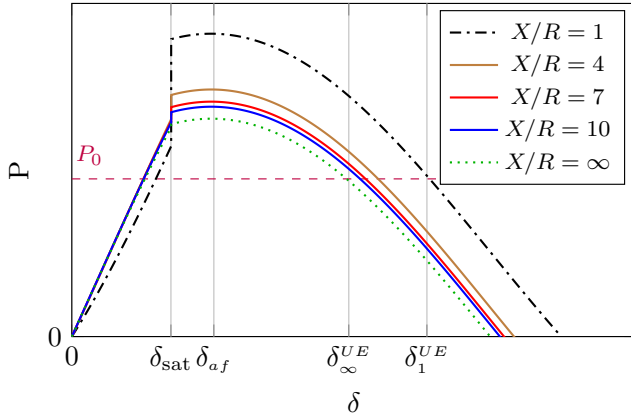


Fig. 11. Power angle curves for different X/R ratios. The GFM IBR is connected to an equivalent impedance of 0.46 p.u., and $D_p = 0.03$ p.u.

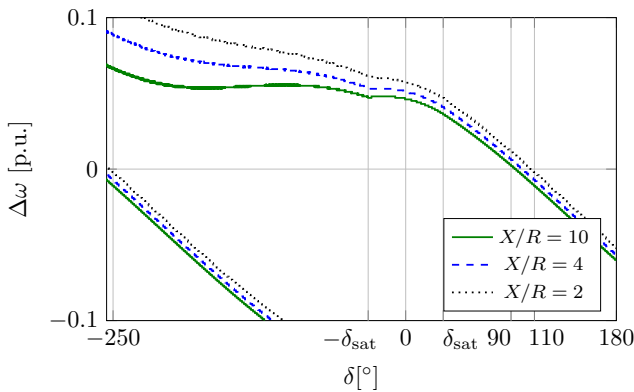


Fig. 12. Borders of DOAs for different X/R ratios. The GFM IBR is connected to an equivalent impedance of 0.46 p.u., and $D_p = 0.03$ p.u.

includes a larger space for smaller values of X/R ratio as in Fig. 12. The DOA of SEP when the GFM IBR is connected to a weaker grid (larger amount of impedance) is smaller compared to those connected to stronger grids according to Fig. 13.

VI. CASE STUDIES

To examine the analyses provided in the previous sections, the system of Fig. 1 with the general parameters of Table. II [4] is simulated in Simulink/MATLAB. It is connected to a grid with the post-fault Thevenin impedance of 0.3 p.u. and X/R ratio of 20 (totally, $Z = 0.46$ p.u.). The following eight cases are simulated:

- Case A: $\beta_A = -6^\circ$, Post-fault angle $\delta_{af} = 34.93^\circ$
- Case B: $\beta_B = -30^\circ$, $\delta_{af} = 34.93^\circ$
- Case C: $\beta_C = -90^\circ$, $\delta_{af} = 34.93^\circ$
- Case D: $\beta_D = -60^\circ$, $\delta_{af} = 44.76^\circ$, $P_0 = 0.2$ p.u.
- Case E: $\beta_E = -60^\circ$, $\delta_{af} = 7.93^\circ$, $P_0 = 0.2$ p.u.
- Case F: $\beta_F = -30^\circ$, $\delta_{af} = 62.01^\circ$
- Case G: $\beta_G = -30^\circ$, $\delta_{af} = 67.71^\circ$
- Case H: Unsaturated current, $\delta_{af} = 76.10^\circ$

Cases A, B, and C are compared to each other to demonstrate the effect of β on post-fault recovery and transient stability. Cases D and E are compared to each other to investigate the risk of locking in the current-saturation mode when the post-fault angle is out of $\mathcal{R} \cup \mathcal{S}$. Cases F, G, and H are compared to show a reduction in DOA caused by the current saturation.

According to Fig. 14, the inverter's output current is limited to 1.2 p.u. for three cases A, B, and C. Among the three

TABLE II
PARAMETERS OF THE SIMULATED GFM FARM.

Param.	Values	Units	Descriptions
S_b	310	MVA	Nominal apparent power
V_b	400	V	Nominal Voltage
V_{dc}	1200	V	DC link voltage
P_0	0.871	p.u.	Active power reference
n	816	-	Number of parallel GFM IBRs
f_n	60	Hz	Nominal frequency
D_p	0.03	p.u.	Active droop coefficient
H	2	p.u.	Virtual inertia
$\Delta\omega_{\max}$	0.0066	p.u.	Maximum frequency deviation
V_s^{ref}	1	p.u.	Voltage reference magnitude
I_s^{max}	1.2	p.u.	Maximum allowed current
X_{tr}	0.16	p.u.	Total reactance of transformer windings

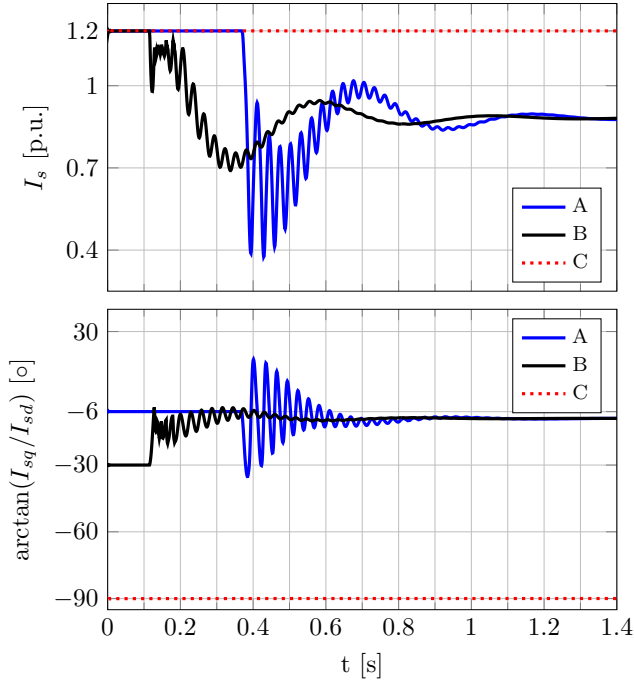


Fig. 14. Simulation results for the post-fault currents in cases A, B, and C.

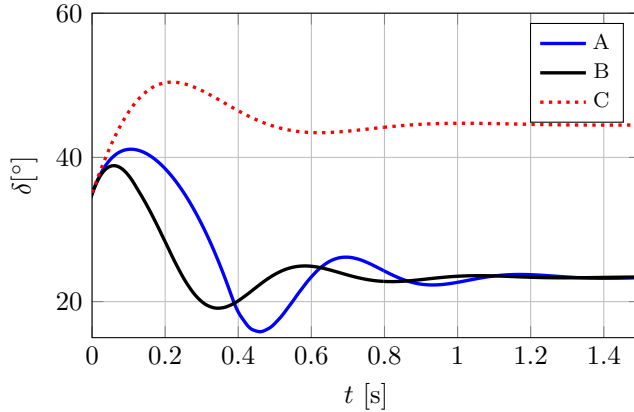


Fig. 15. Simulation results for the post-fault angles in cases A, B, and C.

post-fault trajectories for these cases, case B exhibits the fastest convergence to the SEP as illustrated in Fig. 15. The GFM IBR converges to the SSEP in the case C because $\delta_s^{SE}(\beta_C) = 44.52^\circ \in \mathcal{S}$, and the initial point is within the SSEP's DOA. Since the GFM IBR is locked in the current-saturation mode, it cannot regulate the voltage as shown in Fig. 16. In case A, $\mathcal{R}(\beta_A) = [-23.14^\circ, 23.14^\circ]$ and $\mathcal{S} = [-180^\circ, -32.0455^\circ] \cup [32.0455^\circ, 180^\circ]$. Therefore, after clearing the fault, it stays in the current-saturation mode until the APC angle becomes less than 23.14° at a time around 0.4 s. However, in case B, $\mathcal{R}(\beta_B) = [-45.20^\circ, 45.20^\circ]$. Therefore, oscillations are expected while $32.0455^\circ \leq \delta \leq 45.20^\circ$. These oscillations are reduced using forced saturation introduced in [4]. The GFM IBR operates as a voltage source from 0.2 s. Besides, since $\beta_B < \beta_A < 0$, more post-fault deceleration is

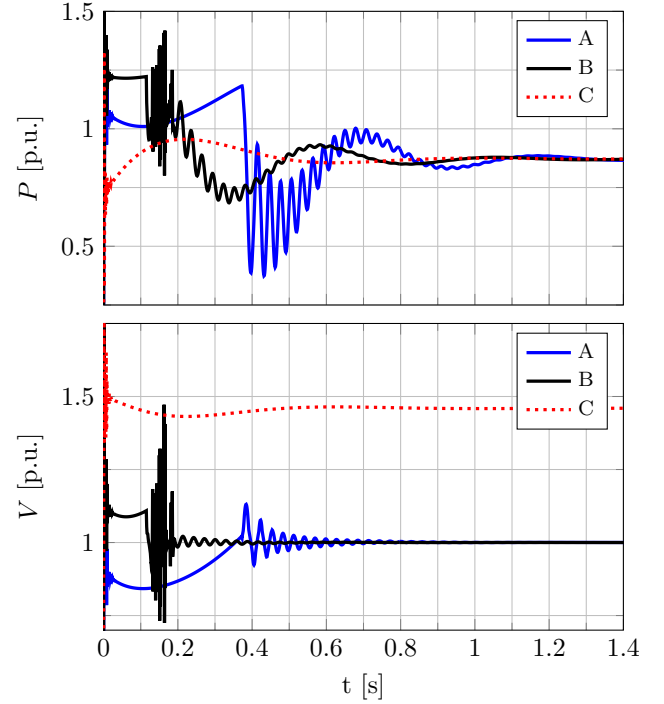


Fig. 16. Simulation results for the post-fault powers and voltages in cases A, B, and C.

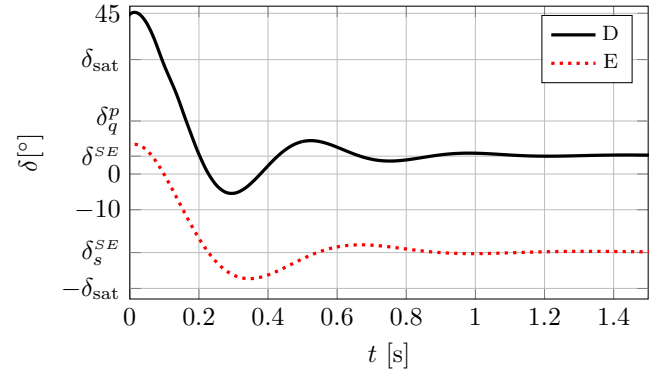


Fig. 17. Simulation results for the post-fault angles in cases D and E.

provided in case B as explained in Section IV. As a result, the angle in case B converges to the SEP faster than case A. Therefore, β should be properly selected in practice so that (a) the GFM IBR does not converge to the SSEP, (b) more post-fault deceleration is provided.

The set of returning angles is $[14.83^\circ, 165.1604^\circ]$ for Cases D and E. The post-fault APC angle is 44.76° for Case C. The GFM IBR returns to the normal operation mode with some oscillations and converges to the SEP as shown in Fig. 17. However, in Case E, the post-fault angle is 7.93° which is out of both $\mathcal{R}(\beta_E)$ and \mathcal{S} . Therefore, it remains in the current-saturation mode as it was during the fault disturbance. Since the power output in the current-saturation mode is more than the power reference at this APC angle, the GFM IBR reduces

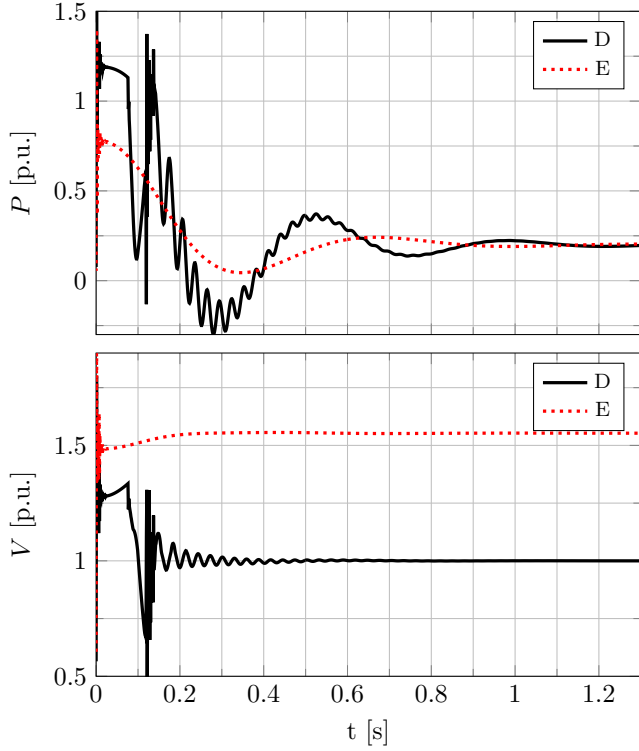


Fig. 18. The post-fault power and voltage in cases D and E.

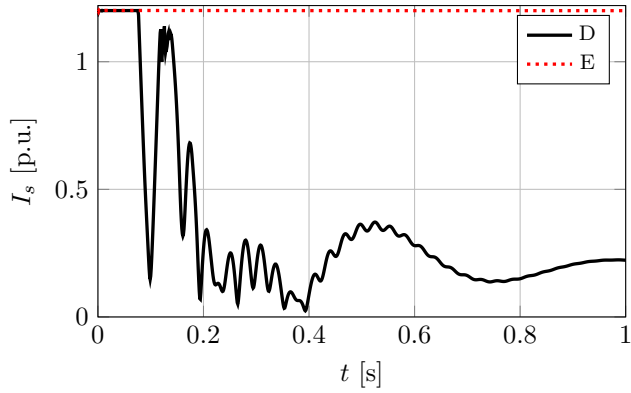


Fig. 19. The post-fault current in cases D and E.

its angle until it converges to the SSEP, which is out of \mathcal{S} , as depicted in Fig. 17. According to Fig. 18 in both Cases the active power output will be the power reference in the steady state. However, the goal of voltage regulation is achieved only in Case D. Fig. 19 also confirms that Case E remains in the current-saturation mode.

Notice that in Cases C and E, the GFM IBR converges to the SSEP; however, the contributing factors are different. While the SSEP was inside \mathcal{S} in Case C (condition \mathcal{C}_1 in Section IV), it was out of \mathcal{S} in Case E. Therefore, \mathcal{C}_1 cannot be the reason for locking into the current-saturation mode. Indeed, the GFM IBR is locked into the current-saturation mode due to condition \mathcal{C}_2 . Therefore, it is concluded that if the GFM IBR is being

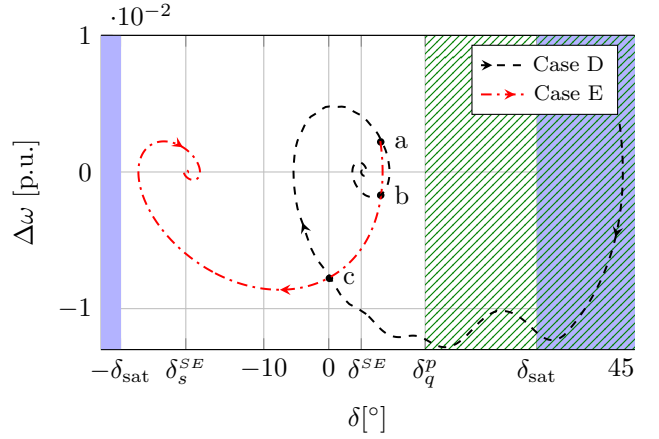


Fig. 20. Post-disturbance trajectories of the GFM IBR in Cases D and E where the solid area and hashed area correspond to the set of entering and returning angles, respectively.

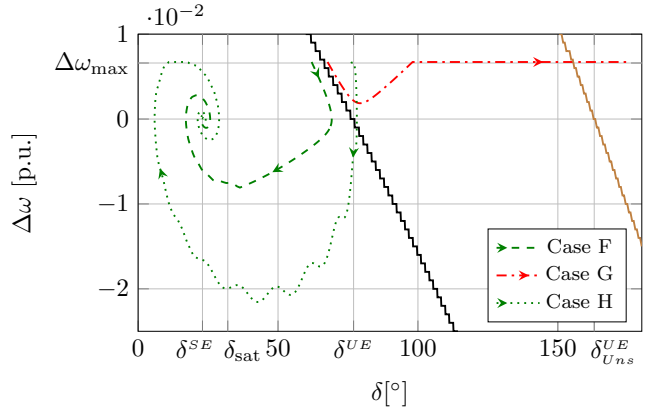


Fig. 21. Post-disturbance trajectories of the GFM IBR in Cases F, G, and H. Black line and brown line are the borders of DOAs for a GFM equipped and not equipped with CRS; respectively.

operated in a light loading, the value of β should be carefully adjusted so that it is not locked into the current-saturation mode after short disturbances.

The dynamic simulations of Cases F and G confirm that the black line in Fig. 21, which is calculated numerically, is the post-fault transient stability border as the black line. This border is much closer to the SEP compared to the border for the unsaturated GFM IBR shown as the brown line in Fig. 21. Simulation of Case H reveals that even though its post-fault angle is larger than Case G, being unsaturated helps its transient stability. However, Fig. 22 shows that an overcurrent significantly exceeding the current limit appears and lasts for a considerable length of time duration in Case H. Therefore, Case H is not practical and it is simulated here only to confirm current saturation deteriorates transient stability.

VII. CONCLUSIONS

A post-disturbance recovery and transient stability analysis for GFM IBRs considering current saturation have been conducted in this paper. It is shown that there is a set of APC

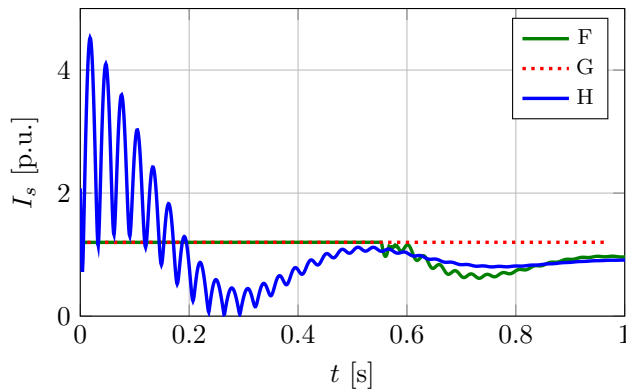


Fig. 22. Post-disturbance current of the GFM IBR in Cases F, G, and H.

angles that GFM IBR returns from the current-saturation in addition to a set of APC angles that GFM IBR enters into the current-saturation mode. These two sets are called sets of returning angles and entering angles. The latter only depends on the grid voltage and impedance, and the former depends on the saturated current angle in addition to the grid voltage and impedance and X/R ratio. It is found that these two sets do not always complement each other.

The GFM IBR may not be able to spontaneously return to SEP subject to certain static and dynamical conditions; instead, there is a risk of being locked into a stable point in current-saturation mode (i.e., SSEP) or even loss of synchronism. The saturated current angle plays a significant role in shaping the post-disturbance dynamics of a GFM IBR and determines the set of returning angles. So, it is crucial to properly select the saturated current angle to mitigate the risk of convergence to the SSEP or instability.

It is shown that there might be cases in which even a very short-time fault disturbance results in the convergence to the SSEP, due to the condition C_2 . Therefore, the traditional CCT or DOA analyses, which are commonly used for transient stability assessment, should be revisited according to the complex behavior of GFM IBRs equipped with current saturation.

ACKNOWLEDGMENTS

The authors would like to thank Prof. Yusheng Xue and Prof. Damiano Varagnolo for their invaluable feedback and suggestions.

REFERENCES

- [1] R. H. Lasseter, Z. Chen and D. Pattabiraman, "Grid-Forming Inverters: A Critical Asset for the Power Grid," in *IEEE Journal of Emerging and Selected Topics in Power Electronics*, vol. 8, no. 2, pp. 925-935, June 2020, doi: 10.1109/JESTPE.2019.2959271.
- [2] H. Zhang, W. Xiang, W. Lin and J. Wen, "Grid Forming Converters in Renewable Energy Sources Dominated Power Grid: Control Strategy, Stability, Application, and Challenges," in *Journal of Modern Power Systems and Clean Energy*, vol. 9, no. 6, pp. 1239-1256, November 2021, doi: 10.35833/MPCE.2021.000257.
- [3] M. H. Ravanji, W. Zhou, N. Mohammed and B. Bahrani, "Comparative Analysis of the Power Output Capabilities of Grid-Following and Grid-Forming Inverters Considering Static, Dynamic, and Thermal Limitations," *IEEE Trans. Power Syst.*, early access, 2023, doi: 10.1109/TPWRS.2023.3279373

- [4] A. Arjomandi-Nezhad, Y. Gu, B. Pal, and D. Varagnolo, "A Model Predictive Approach for Enhancing Transient Stability of Grid-Forming Converters," *IEEE Trans. Power Syst.*, early access, 2024.
- [5] K.V. kkuni, and Y. Guangya, "Effects of current limit for grid forming converters on transient stability: analysis and solution," *arxiv preprint*, arXiv:2106.13555, June 2021.
- [6] C. Luo, X. Ma, T. Liu, X. Wang "Controller-Saturation-Based Transient Stability Enhancement for Grid-Forming Inverters," *IEEE Trans. Power Electron.*, vol. 38, no. 2, pp. 2646-2657. 2022
- [7] J. Lei, X. Xiang, B. Liu, W. Li, and X. He, "Quantitative and Intuitive VSG Transient Analysis with the Concept of Damping Area Approximation," *IEEE Trans. Smart Grid*, Mar 2023.
- [8] X. Fu, J. Sun, M. Huang, Z. Tian, H. Yan, H. Ho-Ching Iu, P. Hu, and X. Zha. "Large-signal stability of grid-forming and grid-following controls in voltage source converter: A comparative study," *IEEE Trans. Power Electronics*, vol. 36, no. 7 7832-7840, 2020.
- [9] J. Lei, X. Xiang, B. Liu, W. Li, and X. He, "The analysis and calculation of power angle dynamics in grid forming converter under large disturbances based on KBM asymptotic method," *IEEE Trans. Power Electronics*, vol. 38, no. 2, 1494-1508, 2022.
- [10] X. He, L. Huang, I. Subotić, V. Häberle, and F. Dörfler, "Quantitative Stability Conditions for Grid-Forming Converters With Complex Droop Control," *arXiv preprint*, arXiv:2310.09933, 2023.
- [11] T. Liu, X. Wang, F. Liu, K. Xin, and Y. Liu, "Transient stability analysis for grid-forming inverters transitioning from islanded to grid-connected mode," *IEEE Open Journal of Power Electronics*, 3, 419-432, 2022.
- [12] J. Lei, X. Xiang, B. Liu, W. Li, X. He, "Transient Stability Analysis of Grid forming Converters based on Damping Energy Visualization and Geometry Approximation," *IEEE Trans. Ind. Electronics*, 2023.
- [13] G. M. Gomes Guerreiro, R. Sharma, F. Martin, P. Ghimire and G. Yang, "Concerning Short-Circuit Current Contribution Challenges of Large-Scale Full-Converter Based Wind Power Plants," in *IEEE Access*, vol. 11, pp. 64141-64159, 2023.
- [14] B. Fan, T. Liu, F. Zhao, H. Wu and X. Wang, "A Review of Current-Limiting Control of Grid-Forming Inverters Under Symmetrical Disturbances," *IEEE Open Journal of Power Electronics*, vol. 3, pp. 955-969, 2022, doi: 10.1109/OJPEL.2022.3227507.
- [15] S. H. Khan, M. Z. Lazkano, P. Izurza, A. Sanchez-Ruiz, J. C. Aceña and J. Arza, "Synchronization Stability of a Grid Forming Converter Under the Effect of Current Limit in Voltage Dips with VI Based Current Limiting Method: Analysis and Solution," *2022 24th European Conference on Power Electronics and Applications (EPE'22 ECCE Europe)*, Hanover, Germany, pp. P.1-P.9, 2022.
- [16] T. Qoria, F. Gruson, F. Colas, G. Denis, T. Prevost and X. Guillaud, "Critical Clearing Time Determination and Enhancement of Grid-Forming Converters Embedding Virtual Impedance as Current Limitation Algorithm," *IEEE Journal of Emerging and Selected Topics in Power Electronics*, vol. 8, no. 2, pp. 1050-1061, June 2020, doi: 10.1109/JESTPE.2019.2959085.
- [17] X. Xiong, C. Wu and F. Blaabjerg, "Effects of Virtual Resistance on Transient Stability of Virtual Synchronous Generators Under Grid Voltage Sag," *IEEE Transactions on Industrial Electronics*, vol. 69, no. 5, pp. 4754-4764, May 2022, doi: 10.1109/TIE.2021.3082055.
- [18] T. Qoria, F. Gruson, F. Colas, X. Kestelyn, and X. Guillaud, "Current limiting algorithms and transient stability analysis of grid-forming VSCs," *Electr. Power Syst. Res.*, vol. 189, p. 106726, 2020.
- [19] G. Wang, L. Fu, Q. Hu, C. Liu and Y. Ma, "Transient Synchronization Stability of Grid-Forming Converter During Grid Fault Considering Transient Switched Operation Mode," *IEEE Trans. Sust. Energy*, vol. 14, no. 3, pp. 1504-1515, July 2023, doi: 10.1109/TSTE.2023.3236950.
- [20] S.P. Me, M.H. Ravanji, B. Leonardi, D. Ramasubramanian, J. Ma, S. Zabihi, and B. Bahrani, "Transient Stability Analysis of Virtual Synchronous Generator Equipped with Quadrature-Prioritized Current Limiter," *IEEE Trans. Power Electronics*, May 2023.
- [21] E. Rokrok, T. Qoria, A. Bruyere, B. Francois, and X. Guillaud, "Transient stability assessment and enhancement of grid-forming converters embedding current reference saturation as current limiting strategy," *IEEE Trans. Power Syst.*, vol. 37, no. 2, pp. 1519-1531, Mar 2022.
- [22] B. Fan and X. Wang, "Fault Recovery Analysis of Grid-Forming Inverters With Priority-Based Current Limiters," *IEEE Trans. Power Syst.*, doi:10.1109/TPWRS.2022.3221209, 2022.
- [23] A. Yazdani, R. Iravani, "Voltage-sourced converters in power systems: modeling, control, and applications," *John Wiley and Sons*, 2010.
- [24] P. Kundur, *Power System Stability and Control*, New York, NY, USA: McGraw-Hill, 1994.